

Gate-reflectometry dispersive readout of a spin qubit in silicon

A. Crippa,^{1,*} R. Ezzouch,¹ A. Aprá,¹ A. Amisse,¹ L. Hutin,² B. Bertrand,² M. Vinet,² M. Urdampilleta,³ T. Meunier,³ M. Sanquer,¹ X. Jehl,¹ R. Maurand,¹ and S. De Franceschi¹

¹ Univ. Grenoble Alpes, CEA, INAC-PHELIQS, F-38000 Grenoble, France

² CEA, LETI, Minatec Campus, F-38000 Grenoble, France

³ Univ. Grenoble Alpes, CNRS, Grenoble INP, Institut Néel, F-38000 Grenoble, France

Silicon spin qubits have emerged as a promising path to large-scale quantum processors. In this prospect, the development of scalable qubit readout schemes involving a minimal device overhead is a compelling step. Here we report the implementation of gate-coupled rf reflectometry for the dispersive readout of a fully functional spin qubit device. We use a p-type double-gate transistor made using industry-standard silicon technology. The first gate confines a hole quantum dot encoding the spin qubit, the second one a helper dot enabling readout. The qubit state is measured through the phase response of a lumped-element resonator to spin-selective interdot tunneling. The demonstrated qubit readout scheme requires no coupling to a Fermi reservoir, thereby offering a compact and potentially scalable solution whose operation may be extended well above 1 Kelvin.

The recent years have witnessed remarkable progress in the development of semiconductor spin qubits [1–4] with an increasing focus on silicon-based realizations [5–7]. Access to isotopically enriched ²⁸Si has enabled the achievement of very long spin coherence times for both nuclear and electron spins [8–10]. In addition, two-qubit gates with increasing high fidelities were demonstrated in electrostatically defined electron double quantum dots [11, 12].

While further improvements in single- and two-qubit gates can be expected, growing research efforts are now being directed to the realization of scalable arrays of coupled qubits [13–18]. Leveraging the well-established silicon technology may enable facing the scalability challenge, and initiatives to explore this opportunity are on the way [19]. Simultaneously, suitable qubit device geometries need to be developed. One of the compelling problems is to engineer scalable readout schemes. The present work addresses this important issue.

It has been shown that a microwave excitations applied to a gate electrode can be used to drive Rabi oscillations via the electric-dipole spin resonance mechanism [6, 20–22]. The possibility of using gate electrodes also for qubit readout would allow for a compact device layout, with a clear advantage for scalability. Gate reflectometry can probe charge tunneling transitions in a quantum dot system through the dispersive shift of a radiofrequency (rf) resonator connected to a gate electrode [23–26]. If combined to spin-selective tunneling, e.g. due to Pauli spin Blockade in a double quantum dot, this technique can provide a way to measure spin states. Recent experiments have shown single-shot electron spin readout in Si by gate reflectometry [27–29]. Here, we implement rf gate reflectometry in a fully functional spin qubit device with a compact layout. Two gates define an isolated hole DQD, and two distinct electric rf tones (one per gate) allow spin manipulation and dispersive readout. Spin initialization and control are performed without involving any charge reservoir; qubit readout

relies on the spin-dependent phase response at the DQD charge degeneracy point. We assess hole single spin dynamics and show coherent spin control, validating a protocol for complete qubit characterization exploitable in more complex architectures.

The experiment is carried out on a p-type Si transistor fabricated on a silicon-on-insulator 300-mm wafer following a standard CMOS process with enlarged spacers and e-beam defined gates [6]. The device, nominally identical to the one in Fig. 1a, presents two parallel top gates, G_R and G_C , wrapping an etched-nanowire channel. At $T_{\text{base}} = 20\text{ mK}$ we achieve the qubit functionality with source (S) and drain (D) at 0 mV and operating G_C and G_R . The respective DC biases V_C and V_R of these gates tune an isolated hole DQD in the wire. The 'Control' gate G_C can deliver also sub- μs pulses and microwave signals in the GHz range to manipulate the qubit. The 'Readout' gate, G_R , is wire-bonded to a $L = 220\text{ nH}$ surface-mount inductor, which along with the parasitic capacitance C_p forms a tank circuit resonating at $f_0 = 339\text{ MHz}$, where $f_0 = 1/(2\pi\sqrt{LC_p})$. Figure 1b shows the phase ϕ and attenuation A of the reflected signal as a function of the resonator driving frequency f_R . From the slope of the phase trace at f_0 we extract a quality factor $Q_{\text{loaded}} \simeq 18$. The qubit device acts as a variable impedance load for the resonator, implying that the resonant frequency f_0 undergoes a dispersive shift dependent on the state of the qubit. For instance, an increase in the load capacitance brings to a red-shift of f_0 . The experiment is performed by exciting the resonator input at $f_R = f_0 = 339\text{ MHz}$ and power $P_R \approx -110\text{ dBm}$. We measure the phase variation $\Delta\phi$ of the reflected signal isolated from the incoming wave by a directional coupler, amplified by 35 dB at 4 K and demodulated to baseband using homodyne detection.

To determine the charge stability diagram of our quantum dot system, we probe the phase response of the

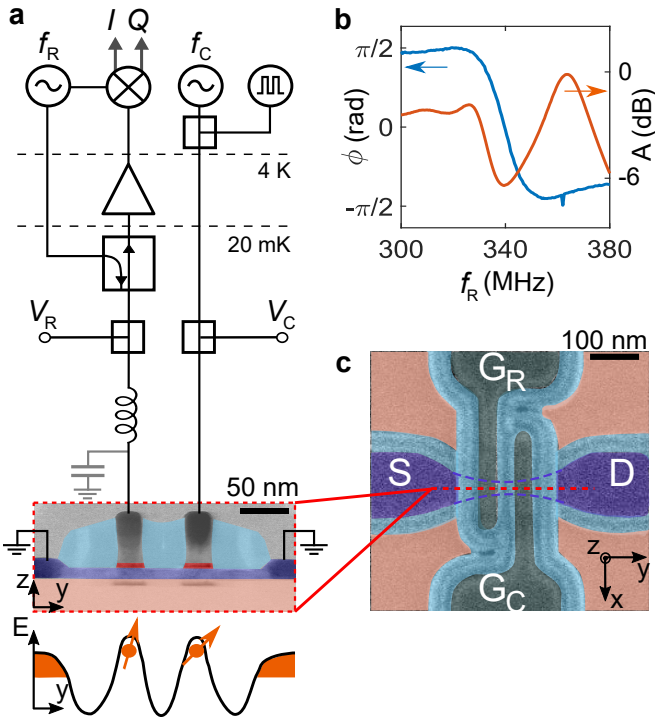


FIG. 1. Device layout and circuitry for qubit dispersive sensing and manipulation. (a) Transmission electron micrograph of a double gate Si device similar to the one measured, with false colors. The Si nanowire (11 nm thick and 15 nm wide, blue) extends between boron-doped source-drain contacts (dark blue) and lies on a SiO₂ substrate (pink). Gates (gray) are 35 nm wide and separated by 35 nm of Si₃N₄ spacers (cyan). At 20 mK the gates tune a hole DQD formed in the active region of the transistor (schematic at the bottom). One gate is connected to a lumped-element resonator excited at frequency f_R by for dispersive readout. A ultra-high frequency digital lock-in demodulates the reflected signal after a directional coupler has separated incoming and outgoing waves and the amplification by a cryo-RF amplifier anchored at the 4 K stage of the dilution refrigerator. The other gate applies pulses and GHz radiation to control the hole spin qubit. (b) Phase response (ϕ) and attenuation (A) of the resonator at base temperature. (c) Scanning electron micrograph of a double gate device. The dashed lines outline the Si nanowire covered by the gates.

resonator while sweeping the DC gate voltages V_R and V_C . The diagonal line in Fig. 2a corresponds to inter-dot charge transitions. The charge stability regions are denoted $(N_1 + 1, N_2)$ and $(N_1, N_2 + 1)$ with two integer numbers N_1 and N_2 counting the equivalent hole occupation in either dot. The reflected signal experiences a phase variation $\Delta\phi$ when the chemical potentials of the two dots are aligned, i.e. detuning $\epsilon = 0$ mV, corresponding to one hole delocalizing across the DQD. The electric dipole of the molecular bonding and anti-bonding states E_{\pm} modifies the impedance of the resonator's load by the quantum capacitance $C_Q = -\alpha^2(\partial^2 E_{\pm}/\partial\epsilon^2)$ [26]. Here α is the lever-arm factor converting the DQD detuning into

energy and it is $\simeq 0.58$ eV/V for the direction marked in Fig. 2a. The width of the detuning trace at $B = 0$ T sets an interdot coupling $t = 7 \pm 1$ μ eV.

The evolution of the interdot line with the B field determines the total charge parity of the DQD and the related spin states [30]. Figure 2b shows the detuning cut ϵ of the interdot signal of panel a) as a function of the magnetic field. Panel c) reports four representative detuning traces from Fig. 2b at zero, weak, moderate and strong magnetic field, $B = 0, 0.355, 0.46$ and 0.85 T respectively. The interdot phase signal progressively drops by increasing B . At $B = 0.355$ T the line profile is slightly asymmetric, while at $B = 0.46$ T two peaks can be distinguished and move apart by rising the magnetic field. Figure 2b-c can be better understood considering the energy diagram of $(0, 2) \leftrightarrow (1, 1)$ equivalent charge states as a function of the detuning ϵ at finite B field presented in Fig. 2d. The spectrum is similar to the one of a singlet-triplet electron DQD [1]. The bare interdot tunneling t sets the spin-conserving transitions rate between the two singlets $S(1, 1)$ and $S(0, 2)$. Different g -factors for left (g_L^*) and right dot (g_R^*) split the $(1, 1)$ energy states in the far-positive detuned region into $|\downarrow\downarrow\rangle, |\uparrow\downarrow\rangle, |\downarrow\uparrow\rangle, |\uparrow\uparrow\rangle$ [21, 31, 32]. At strong negative detuning, the ground state is a spin-singlet state $S(0, 2)$ (the triplet states $T(0, 2)$ are higher in energy and disregarded). Around zero detuning, the antiparallel spin states hybridize into an unpolarized triplet $T_0(1, 1)$ and two molecular singlet states, $S_{g,e}$, bonding and anti-bonding respectively [Suppl. Mat.].

We use the spectrum of Fig. 2d to model the evolution of the interdot phase signal of Fig. 2b-c. The available excited states are considered occupied according to a Boltzmann statistics. Since here we probe a reflectometry signal averaged over many resonator cycles, the experimental phase signal reads $\Delta\phi = \sum_i \langle \Delta\phi \rangle_i$, where $\langle \Delta\phi \rangle_i$ is the thermal averaged phase response associated to the state i [30]. Figure 2e shows $\langle \Delta\phi \rangle$ as a function of detuning ϵ for each energy level of panel d) for an effective temperature $T_{\text{eff}} = 250$ mK. The state $|\downarrow\downarrow\rangle$ corresponds to the triplet $T_-(1, 1)$, is linear in ϵ and does not cause any resonator dispersive shift (same for $|\uparrow\uparrow\rangle$); however, S_g , S_e and $T_0(1, 1)$ possess a curvature and are sensed by the reflectometry apparatus [Suppl. Mat.]. We note that the phase signal relative to $T_0(1, 1)$ has a peak-dip lineshape, whose minimum lies at positive ϵ (blue trace of Fig. 2e), contrary to the minimum of S_g , which is at negative ϵ (green trace of Fig. 2e). In our case $T_0(1, 1)$ and S_g are populated and appear in Fig. 2b as two faint branches raising at $B \sim 0.4$ T. At such a field, having $T_-(1, 1)$ occupied with unit probability would imply $\Delta\phi = 0$ according to the schematics of Fig. 2d.

With $T_{\text{eff}} = 250$ mK we obtain a magnetic field dependence of the interdot phase signal in qualitative agreement with the experimental data (inset in Fig. 2b); Figure 2e also captures the asymmetric line shape at low field

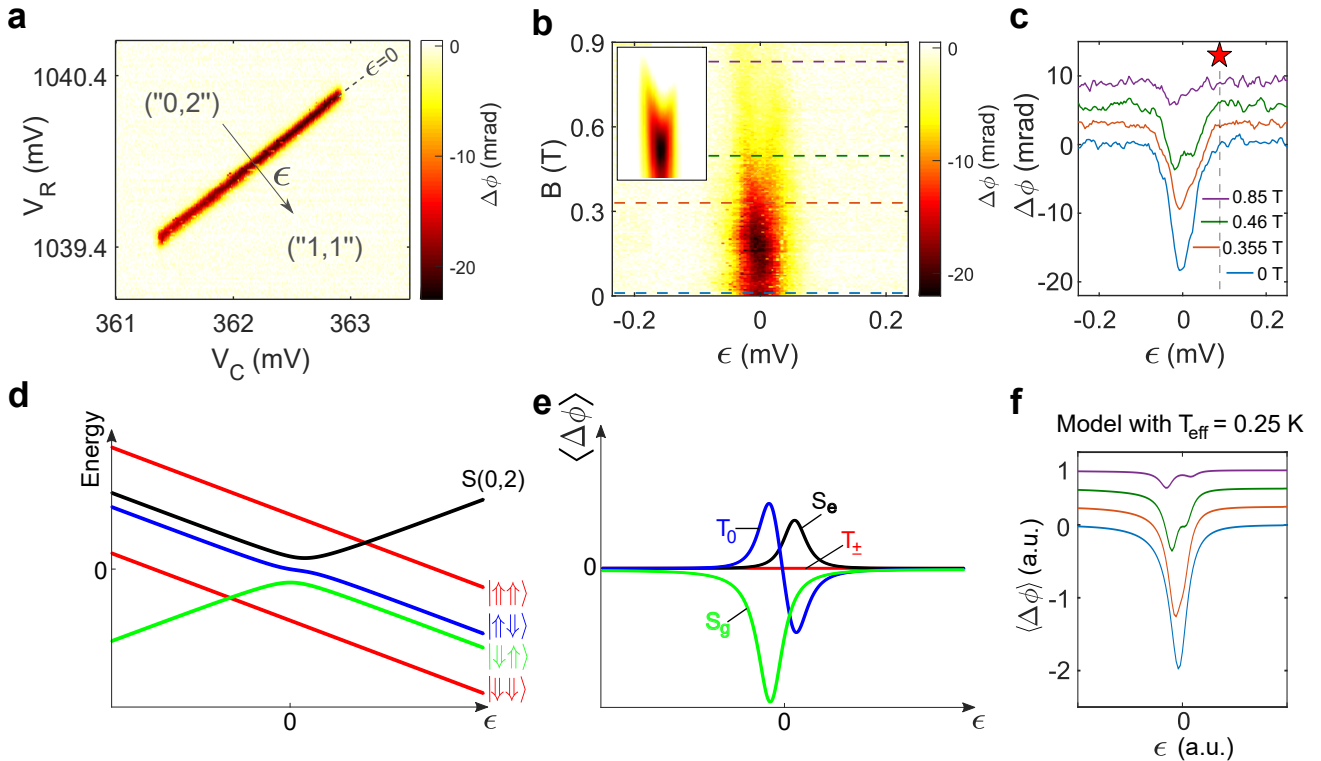


FIG. 2. Magnetspectroscopy of the DQD. (a) Phase shift of the reflected signal as a function of V_C and V_R near the interdot transition line under study. The arrow indicates the detuning axis ϵ . (b) Interdot dispersive signal as a function of the magnetic field. The phase response diminishes by increasing B , a signature of effective $(0, 2) \leftrightarrow (1, 1)$ interdot charge transitions. (c) Phase traces versus detuning at $B = 0, 0.355, 0.46$, and 0.85 T, taken from panel b) at the dashed lines. Data are offset for clarity. (d) Schematic of DQD energy levels of an even parity charge transition at finite B -field with $|g_L^* - g_R^*| = 0.5$. (e) Thermally-averaged phase response $\langle \Delta\phi \rangle$ with $T_{\text{eff}} = 0.25$ K. $\Delta\phi$ is the bare second derivative of the energy bands in panel d). Around $\epsilon = 0$, the measured dispersive shift $\langle \Delta\phi \rangle$ is due to the ground singlet S_g (green), the triplet T_0 (blue) and the excited singlet S_e (black). The polarized triplets T_-, T_+ (red) don't contribute to the dispersive signal. (f) Qualitative phase shift expected from the model of panels d-e), with an effective temperature $T_{\text{eff}} = 0.25$ K. The double peak structure is in accordance with the traces in panel c). Details of the model in Suppl. Mat.

and the appearance of the phase signal from the states S_g and T_0 at $B > 0.4$ T.

Now that we have elucidated the spectroscopy of the DQD, we focus on electrical control and dispersive read-out of single hole spins. Electric dipole spin resonance (EDSR) transitions [6, 22, 33] are induced by a microwave electric field applied at frequency f_C on the 'Control' gate. Figure 3a shows the dispersive signal of a EDSR transition line. The microwave radiation of frequency f_C is applied continuously and B is oriented along the nanowire axis. The DQD is detuned at the red star position in Fig. 2c. At resonance $h f_C = g \mu_B B$ (with h the Planck's constant, μ_B the Bohr magneton and g the effective hole g-factor) the dispersive signal is changed as the states population is modified. The resonance line of Fig. 3a is attributed to a second harmonic driving process ($2h f_C = g \mu_B B$) from which we extract $g = 1.735 \pm 0.002$. The weaker first harmonic signal is shown in the inset of Fig. 3a.

To resolve single spin transitions dispersively, the resonating states must have different quantum capacitances. A careful tuning of the gate voltages allows to optimize the visibility of such EDSR transitions. Figure 3b shows a strip of stability diagram around the DQD charge degeneracy region; the interdot line has a double peak structure, consistently with data in Fig. 2b-c for analogous B field amplitude but with different orientation. The measurement is performed while applying a continuous microwave tone $f_C = 7.42$ GHz. Evidence of EDSR transitions can be seen in Fig. 3b as a distinct phase signal around $V_C \simeq 362.5$ mV and $V_R \simeq 1040$ mV, i.e. slightly inside the $(1, 1)$ charge region, as pinpointed by the black arrow. Such EDSR feature is extremely localized in the stability diagram as the effective g -factor varies with the gate voltages [22].

Figure 3c displays cuts at fixed V_R voltage of the interdot transition line in different conditions. If no microwaves are applied, we see the double-peak line shape discussed

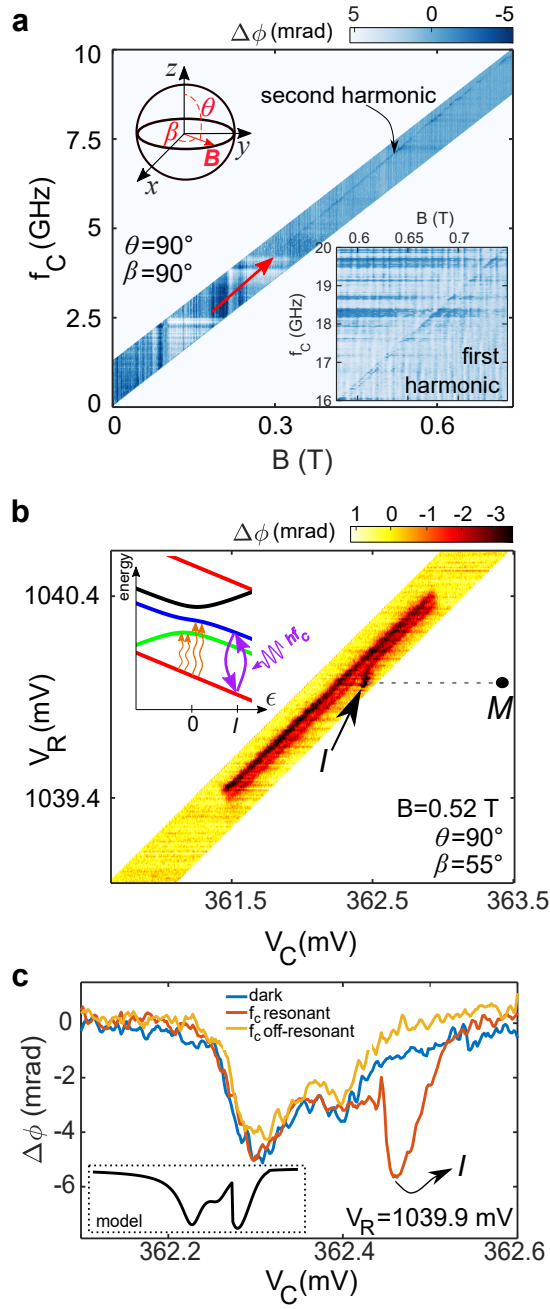


FIG. 3. Microwave and detuning spectroscopy of EDSR transitions. (a) Dispersion response as a function of the EDSR tone f_C and magnetic field B , for first (inset) and second harmonic (main). The phase of the reflected signal changes when the energy of the photon matches the Zeeman splitting of spin states with different C_Q . The field points the y direction with respect to the frame of Fig. 1a. (b) Stability diagram at $B = 0.52$ T (orientation $\beta = 55^\circ$ and $\theta = 90^\circ$) with a microwave tone $f_C = 7.42$ GHz of power $P_C \approx -80$ dBm applied. Transitions from $T_{-}(1,1)$ and $T_0(1,1)$ (purple arrows in inset) are driven at point I , where the excitations due to T_{eff} (orange arrows) are less effective. In the stability diagram, the change of population induced by EDSR stands out as a spot-like tail at point I . (c) Phase shift as a function of V_C without microwave irradiation (dark), $f_C = 7.42$ GHz (in-resonance) and $f_C = 7.6$ GHz (off-resonance), at $V_R = 1039.9$ mV. EDSR-stimulated transitions appear as a pronounced peak (I); position and lineshape are compatible with the model, see inset.

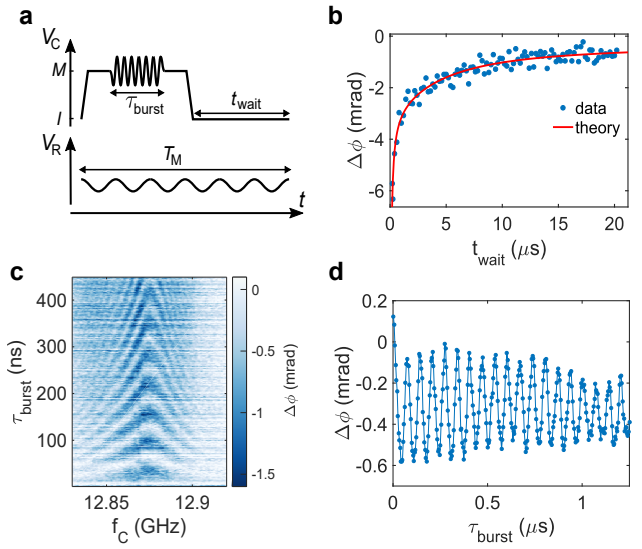


FIG. 4. Single spin control and dispersive sensing. (a) The pulse sequence alternating between Coulomb blockade (M) for manipulation and nearly interdot crossing (I) to reset the spin system. A microwave burst rotates the hole spin during the manipulation stage. The readout tone is applied for the sequence period T_M continuously. (b) Phase shift as a function of t_{wait} for a $\simeq 1$ mV pulse on V_C with $\tau_{\text{burst}} = 50$ ns and $f_C = 12.865$ GHz, with $B = 0.512$ T along $\beta = 0^\circ$ and $\theta = 60^\circ$. The phase signal approaches 0 when $t_{\text{wait}} \gg T_1$. A simple model yields $T_1 = 2.7 \pm 0.7 \mu\text{s}$. (c) Dispersive signal $\Delta\phi(f_C, \tau_{\text{burst}})$, measured with the detuning pulses of panel a) with $t_{\text{wait}} = 1 \mu\text{s}$. 4 maps have been averaged. (d) Phase response as a function of EDSR burst time at $f_C = 12.865$ GHz. The plot shows Rabi oscillations with 15 MHz frequency due to coherent spin rotations. Each data point is integrated for 100 ms and then averaged over 30 traces.

above. At $V_C \simeq 362.45$ mV, the spin resonance condition is met for $f_C = 7.42$ GHz (red trace), and a strong signal appears, corresponding to point I in Fig. 3b. The peak disappears by changing f_C by 20 MHz (cyan trace). At point I , resonant microwave excitation enables the spectroscopy of the $T_0(1,1)$ state. The inset shows the signal we expect from our model. In a small detuning window, the populations of $T_{-}(1,1)$ and $T_0(1,1)$ are supposed balanced by EDSR (see the energy levels in the inset of Fig. 3b); this results in a phase signal dramatically enhanced resembling the feature centered at I in the main panel. A further confirmation that the spin transitions are driven between $T_{-}(1,1)$ and $T_0(1,1)$ is given by the extrapolated intercept at 0 T of the EDSR transition line in Fig. 3a, found much smaller (< 100 MHz) than t . In the following, we utilize point I to perform qubit readout.

The device is operated as a spin qubit implementing the protocol outlined in Fig. 4a. The voltage sequence in the upper part of Fig. 4a tunes the DQD at point M , i.e. deep in the $(1,1)$ stability region, where either hole is largely localized in one dot and decoupled from

the other. A microwave burst of duration τ_{burst} and frequency f_C drives single spin rotations between $|\downarrow\downarrow\rangle$ and $|\uparrow\downarrow\rangle$; the system is then brought back to I for a time t_{wait} for initialization. The readout eventually relies on the spin-resolved phase shift at I , though the reflectometry tone f_R is applied during the whole sequence period T_M and the reflected signal is streamed constantly to the acquisition module.

First, we determine the spin state lifetime T_1 at the readout point I by sweeping t_{wait} after a π -burst at point M . The data are shown in Fig. 4b. The phase signal rapidly diminishes with increasing t_{wait} as relaxations progressively populate the non-dispersive state $T_-(1,1)$. Fit to theory yields a lifetime $T_1 = 2.7 \pm 0.7 \mu\text{s}$.

We demonstrate coherent single spin control in the chevron plot of Fig. 4c. It shows the phase signal collected as a function of microwave burst time τ_{burst} and driving frequency f_C . The spin state is initialized at point I ($t_{\text{wait}} \sim T_1$). In Fig. 4d the phase signal is plotted as a function of τ_{burst} with f_C set at the Larmor frequency. The Rabi oscillations have 15 MHz frequency, consistently with Refs. 6 and 22. Data have been averaged over 30 measurements though the oscillations are easily distinguishable from single scans where each point is integrated over 100 ms. Figure 4 witnesses the success in using electrical rf signals both for coherent manipulation by EDSR and for qubit-state readout by means of gate reflectometry.

The measured T_1 is compatible with the relaxation times obtained for hole singlet-triplet states in acceptor pairs in Si [34] and in Ge/Si nanowire double quantum dots [35]; in both cases T_1 has been measured at the charge degeneracy point with reflectometry setups similar to ours. Nonetheless, charge detector measurements have shown T_1 approaching 100 μs for single hole spins in Ge hut wire quantum dots [36] and $\lesssim 1 \text{ ms}$ for Ge/Si singlet-triplet systems [37]. This suggests that despite the intrinsic spin-orbit coupling single spin lifetimes in the ms range might be achievable in Si too. A strategy to boost T_1 at the readout point may consist of inserting rf isolators between the coupler and the amplifier to reduce the backaction on the qubit.

We note that T_1 could depend on the orientation of the magnetic field as well. Future studies on magnetic field anisotropy will clarify whether T_1 , along with the effective g-factors (and hence the quantum capacitance for dispersive readout) and Rabi frequency, can be maximized at once along a specific direction.

The gate-based dispersive sensing demonstrated does not require local reservoirs of charges or embedded charge detectors. Frequency multiplexing can be applied, thus allowing qubit readout in 2D quantum dot arrays even at temperatures above 1 K.

* alessandro.crippa@cea.fr or romain.maurand@cea.fr

- [1] J. R. Petta, A. C. Johnson, J. M. Taylor, E. A. Laird, A. Yacoby, M. D. Lukin, C. M. Marcus, M. P. Hanson, and A. C. Gossard, *Science* **309**, 2180 (2005).
- [2] E. A. Laird, F. Pei, and L. Kouwenhoven, *Nature nanotechnology* **8**, 565 (2013).
- [3] M. G. Dutt, L. Childress, L. Jiang, E. Togan, J. Maze, F. Jelezko, A. Zibrov, P. Hemmer, and M. Lukin, *Science* **316**, 1312 (2007).
- [4] H. Watzinger, J. Kukucka, L. Vukušić, F. Gao, T. Wang, F. Schäffler, J.-J. Zhang, and G. Katsaros, *Nature communications* **9**, 3902 (2018).
- [5] E. Kawakami, P. Scarlino, D. R. Ward, F. Braakman, D. Savage, M. Lagally, M. Friesen, S. N. Coppersmith, M. A. Eriksson, and L. Vandersypen, *Nature nanotechnology* **9**, 666 (2014).
- [6] R. Maurand, X. Jehl, D. Kotekar-Patil, A. Corna, H. Bohuslavskyi, R. Laviéville, L. Hutin, S. Barraud, M. Vinet, M. Sanquer, and S. De Franceschi, *Nature Comm.* **7**, 13575 (2016).
- [7] M. Reed, B. Maune, R. Andrews, M. Borselli, K. Eng, M. Jura, A. Kiselev, T. Ladd, S. Merkel, I. Milosavljevic, E. Pritchett, M. Rakher, R. Ross, A. Schmitz, A. Smith, J. Wright, M. Gyure, and H. AT, *Physical review letters* **116**, 110402 (2016).
- [8] M. Veldhorst, J. C. C. Hwang, C. H. Yang, A. W. Leenstra, B. De Ronde, J. P. Dehollain, J. T. Muhonen, F. E. Hudson, K. M. Itoh, A. Morello, and A. S. Dzurak, *Nature Nanotech.* **9**, 981 (2014).
- [9] J. T. Muhonen, J. P. Dehollain, A. Laucht, F. E. Hudson, R. Kalra, T. Sekiguchi, K. M. Itoh, D. N. Jamieson, J. C. McCallum, A. S. Dzurak, *et al.*, *Nature nanotechnology* **9**, 986 (2014).
- [10] J. Yoneda, K. Takeda, T. Otsuka, T. Nakajima, M. R. Delbecq, G. Allison, T. Honda, T. Kidera, S. Oda, Y. Hoshi, *et al.*, *Nature nanotechnology* **13**, 102 (2018).
- [11] D. M. Zajac, A. J. Sigillito, M. Russ, F. Borjans, J. M. Taylor, G. Burkard, and J. R. Petta, *Science* **359**, 439 (2018).
- [12] T. Watson, S. Philips, E. Kawakami, D. Ward, P. Scarlino, M. Veldhorst, D. Savage, M. Lagally, M. Friesen, S. Coppersmith, *et al.*, *Nature* **555**, 633 (2018).
- [13] M. Veldhorst, H. Eenink, C. Yang, and A. Dzurak, *Nature communications* **8**, 1766 (2017).
- [14] R. Li, L. Petit, D. P. Franke, J. P. Dehollain, J. Helsen, M. Steudtner, N. K. Thomas, Z. R. Yoscovits, K. J. Singh, S. Wehner, *et al.*, *Science advances* **4**, eaar3960 (2018).
- [15] C. Jones, M. A. Fogarty, A. Morello, M. F. Gyure, A. S. Dzurak, and T. D. Ladd, *Physical Review X* **8**, 021058 (2018).
- [16] D. Zajac, T. Hazard, X. Mi, E. Nielsen, and J. Petta, *Physical Review Applied* **6**, 054013 (2016).
- [17] L. Vandersypen, H. Bluhm, J. Clarke, A. Dzurak, R. Ishihara, A. Morello, D. Reilly, L. Schreiber, and M. Veldhorst, *npj Quantum Information* **3**, 34 (2017).
- [18] P. Pakkiam, M. G. House, D. M. Koch, and M. Y. Simmons, *Nano letters* (2018).
- [19] L. Hutin, B. Bertrand, R. Maurand, A. Crippa, M. Ur-dampilletta, Y. Kim, A. Amisse, H. Bohuslavskyi, L. Bourdet, S. Barraud, *et al.*, in *2018 48th ESSDERC*

(IEEE, 2018) pp. 12–17.

[20] K. Nowack, F. Koppens, Y. V. Nazarov, and L. Vandersypen, *Science* **318**, 1430 (2007).

[21] K. Petersson, L. McFaul, M. Schroer, M. Jung, J. M. Taylor, A. A. Houck, and J. Petta, *Nature* **490**, 380 (2012).

[22] A. Crippa, R. Maurand, L. Bourdet, D. Kotekar-Patil, A. Amisse, X. Jehl, M. Sanquer, R. Laviéville, H. Bohuslavskyi, L. Hutin, S. Barraud, M. Vinet, Y. Niquet, and S. De Franceschi, *Physical review letters* **120**, 137702 (2018).

[23] C. Ciccarelli and A. Ferguson, *New Journal of Physics* **13**, 093015 (2011).

[24] J. Colless, A. Mahoney, J. Hornibrook, A. Doherty, H. Lu, A. Gossard, and D. Reilly, *Physical review letters* **110**, 046805 (2013).

[25] M. Gonzalez-Zalba, S. Barraud, A. Ferguson, and A. Betz, *Nature communications* **6**, 6084 (2015).

[26] A. Crippa, R. Maurand, D. Kotekar-Patil, A. Corna, H. Bohuslavskyi, A. O. Orlov, P. Fay, R. Laviéville, S. Barraud, M. Vinet, *et al.*, *Nano letters* **17**, 1001 (2017).

[27] P. Pakkiam, A. Timofeev, M. House, M. Hogg, T. Kobayashi, M. Koch, S. Rogge, and M. Simmons, *arXiv preprint arXiv:1809.01802* (2018).

[28] A. West, B. Hensen, A. Jouan, T. Tanttu, C. Yang, A. Rossi, M. Gonzalez-Zalba, F. Hudson, A. Morello, D. Reilly, *et al.*, *arXiv preprint arXiv:1809.01864* (2018).

[29] M. Urdampilleta, D. J. Niegemann, E. Chanrion, B. Jadot, C. Spence, P.-A. Mortemousque, L. Hutin, B. Bertrand, S. Barraud, R. Maurand, *et al.*, *arXiv preprint arXiv:1809.04584* (2018).

[30] M. Schroer, M. Jung, K. Petersson, and J. Petta, *Physical review letters* **109**, 166804 (2012).

[31] S. Nadj-Perge, S. Frolov, E. Bakkers, and L. P. Kouwenhoven, *Nature* **468**, 1084 (2010).

[32] S. Nadj-Perge, V. Pribiag, J. Van den Berg, K. Zuo, S. Plissard, E. Bakkers, S. Frolov, and L. Kouwenhoven, *Phys. Rev. Lett.* **108**, 166801 (2012).

[33] B. Venitucci, L. Bourdet, D. Pouzada, and Y.-M. Niquet, *Physical Review B* **98**, 155319 (2018).

[34] J. van der Heijden, T. Kobayashi, M. House, J. Salfi, S. Barraud, R. Laviéville, M. Simmons, and S. Rogge, *arXiv preprint arXiv:1703.03538* (2017).

[35] A. P. Higginbotham, T. W. Larsen, J. Yao, H. Yan, C. M. Lieber, C. M. Marcus, and F. Kuemmeth, *Nano letters* **14**, 3582 (2014).

[36] L. Vukušić, J. Kukučka, H. Watzinger, F. Schäffler, and G. Katsaros, *Nano Letters* (2018).

[37] Y. Hu, F. Kuemmeth, C. M. Lieber, and C. M. Marcus, *Nature nanotechnology* **7**, 47 (2012).